Published in final edited form as:
J Vasc Interv Radiol. 2012 March ; 23(3): 385–395. doi:10.1016/j.jvir.2011.11.018.

Development and Preliminary Testing of a Translational Model of Hepatocellular Carcinoma for Magnetic Resonance Imaging and Interventional Oncologic Investigations

Scott M. Thompson, B.A.,
Medical Scientist Training Program, Mayo Clinic

Matthew R. Callstrom, M.D., Ph.D.,
Department of Radiology, Mayo Clinic

Bruce Knudsen, M.S.,
Department of Laboratory Medicine and Pathology, Mayo Clinic

Jill L. Anderson,
Division of Physiology and Bioengineering, Mayo Clinic

Rickey E. Carter, Ph.D.,
Division of Health Sciences Research, Mayo Clinic

Joseph P. Grande, M.D., Ph.D.,
Department of Laboratory Medicine and Pathology, Mayo Clinic

Lewis R. Roberts, M.B., Ch.B., Ph.D., and
Division of Gastroenterology and Hepatology, Mayo Clinic

David A. Woodrum, M.D., Ph.D.
Department of Radiology, Mayo Clinic

Abstract

Purpose—To develop a translational rat hepatocellular carcinoma (HCC) disease model for magnetic resonance imaging and image-guided interventional oncologic investigations.

Corresponding Author: David A. Woodrum., Department of Radiology, Mayo Clinic, 200 First Street Southwest, Rochester, MN 55905, USA, Fax: (507) 255-7872, Phone: (507) 255-7208, woodrum.david@mayo.edu.

Institution
College of Medicine, Mayo Clinic, 200 First Street Southwest, Rochester, MN 55905, USA

Financial Disclosures

Regarding disclosures, Mr. Scott Thompson has received a research grant from the SIR Foundation (SIR Allied Scientist Training Grant); Dr. David Woodrum has received a research grant from Visualase, Inc. and an RSNA Research Scholar Grant; and Dr. Matthew Callstrom has received research grants from Endocare, Inc., and Siemens AG.

Conflicts of Interest

The authors report no conflicts of interest and have conducted this research in compliance with institutional ethical and regulatory guidelines.

SIR Annual Meeting

Not presented

Methods and Materials—Male rats underwent sham control surgery (N=6), selective bile duct ligation (SBDL; N=4) or common bile duct ligation (CBDL; N=6) with procedure optimization in 4 rats and N1S1 cell injection into 2–3 sites in the liver of 12 rats. All rats subsequently underwent MRI to assess tumor establishment and volume. Mesenteric angiography and percutaneous MR-guided laser ablation of the liver were performed in a subgroup of animals (N=4). Animal weight and liver tests were monitored. After harvesting, the livers were subjected to gross and microscopic analysis. Tumor volume and laboratory parameters were assessed between ligation groups.

Results—MRI demonstrated hyperintense T2 and hypointense T1 lesions with tumor induction in 5/10 (50.0%), 7/8 (87.5%) and 12/12 (100%) sites in the control, SBDL and CBDL groups, respectively. Tumor volumes differed significantly by group ($p<0.02$). Mesenteric angiography demonstrated an enhancing tumor stain. Clinical and laboratory assessment revealed a significant decrease in weight ($p = 0.01$) and albumin ($p<0.01$) and increase in total bilirubin ($p = 0.02$) in CBDL rats but not SBDL rats ($p=1.0$). Histologic examination showed high-grade HCCs with local and vascular invasion within the context of early fibrosis in CBDL and SBDL rats. MR-guided laser ablation generated a 1–2 cm ablation zone with histology consistent with reversible and irreversible injury.

Conclusion—A biologically relevant rat hepatocellular carcinoma disease model was developed for MR imaging and preliminary interventional oncologic applications.

INTRODUCTION

With the rapid increase in interventional oncologic treatments for hepatocellular carcinoma (HCC), the need for translational animal tumor models is critical to better understand the complex interactions between thermal- and chemo-ablative therapies and the molecular mechanisms of HCC sensitivity or resistance to cellular death and clinical recurrence. HCC is representative of the current limitations for animal models in the field of interventional oncology (1, 2). The porcine model is the most representative of the human liver for organ and vessel size but there is no cost-effective or reproducible tumor model in pigs (3). The rabbit liver VX-2 and rat R3230 mammary adenocarcinoma tumor models have served as important models for interventional oncologic studies but are limited in their translational applicability to HCC (1, 2, 4). More recently, two different orthotopic rat HCC models have been described including the Buffalo rat with implanted McA-RH7777 hepatoma cell line (5) and the Sprague-Dawley rat with implanted Novikoff N1S1 hepatoma cell line, the latter of which has emerged as a feasible model in the liver for catheter-directed chemotherapy, Y-90 administration, and percutaneous irreversible electroporation (6–9).

HCC represents two distinct diseases: liver dysfunction and malignancy. Emerging evidence suggests that underlying liver disease is a critical modulator of hepatocarcinogenesis and tumor progression (10, 11). With the Sprague-Dawley rat, it has been shown that cirrhosis can be produced with common bile duct ligation and that tumors implanted in the cirrhotic liver progress more rapidly (12, 13). Understanding how the background fibrotic liver microenvironment affects HCC tumorigenesis and ablation resistance is imperative for improving interventional oncology therapies (14). Therefore there is a critical need for a biologically relevant, clinically translational model of HCC for pre-clinical studies testing novel interventional oncologic synergistic therapies as well mechanistic studies into the role of the tumor biology and microenvironment on treatment efficacy and tumor progression.

The aim of this investigation was to develop a translational orthotopic, syngeneic immunocompetent rat HCC disease model for MR imaging and preliminary image-guided percutaneous and catheter-based interventional oncologic investigations.

MATERIALS AND METHODS

All studies were approved by the Institutional Animal Care and Use Committee (IACUC) and conducted in accordance with institutional guidelines.

Cell Culture

N1S1 rat liver cancer cells (ATCC CRL-1603, Manasas, VA) were maintained in suspension culture flasks in complete media per manufacturer instructions, incubated at 37°C and 5% CO_2 and passaged three times per week.

Rats

16 male Sprague-Dawley rats (Charles River, Wilmington, MA) weighing 400–450 grams were used in this study. Rats were housed in individual cages in a climate controlled setting with access to food and water *ad libetem* and maintained on a 12-hour light/dark cycle. 4 rats were used for initial procedure optimization and development of imaging sequences and the subsequent 12 rats were included in the model development.

Surgery

Rats were anesthetized with an intraperitoneal injection of Ketamine (40–80mg/kg) and Xylazine (5–10mg/kg), shaved and prepped with iodine swabs and placed on a warmed (37°C) surgical stage for surgery using a Leica MZ 12.5 operating microscope (Leica Microsystems, Heerbrug, Switzerland). A vertical midline abdominal incision was made and the rats underwent one of the following bile duct ligation procedures(15): *Common Bile Duct Ligation (CBDL) (N=6):* Common bile duct (CBD) was identified, triply tied with 2-0 silk suture and cut (Figure 1a). *Selective Bile Duct Ligation (SBDL) (N=4):* The segmental branch of the common bile duct supplying the middle hepatic lobe (MHL) or left lateral lobe (LLL) was identified and doubly tied (Figure 1b). *Sham Control (Normal) (N=6*): In six rats the bile duct was mobilized but no surgical ligation was performed. CBDL and SBDL rats were given a subcutaneous injection of 50mcg of vitamin K (Bimeda-MTC Animal Health Inc., Cambridge, Ontario) prior to surgery and once per week thereafter to prevent vitamin K deficiency and bleeding diasthesis (15).

Cell Inoculation

At the time of surgery, 1×10^6 cells in 150–200μl of complete media were injected using a 22-gauge needle into two or three subcapsular sites in the liver (left lateral lobe, right middle lobe and/or left idle lobe) in CBDL (N=4) and control rats (N=4), while two sites (left middle lobe and left lateral lobe) were injected in SBDL rats (N=4), one in the ligated lobe and one in the non-ligated lobe.

Imaging

Magnetic Resonance Imaging—7-days following cell inoculation, 12 rats were anesthetized, secured to an MR compatible board and placed in a BC-10 wrist coil, manufactured by the institutional MRI Research lab. A 25-gauge tail vein catheter was inserted for injection of contrast. The rats were imaged using a 3.0T MR scanner (GE Medical Inc., Milwaukee, WI) with non-contrast-enhanced Fast Spin Echo (FSE) T1 and T2 and gadolinium enhanced FSE T1 and/or spoiled gradient echo (SPGR) imaging in three planes. Magnevist® gadopentetate dimeglumine contrast agent (Bayer Schering Pharma, Berlin, Germany) was manually injected at a dose of 0.1mmol/kg through the tail vein catheter. Tumor induction and dimensions were measured from the FSE T2 images in the axial, coronal or sagital planes by an MR radiologist blinded to the study groups. Tumor volumes were calculated using the formula for an ellipsoid by multiplying the maximum longitudinal diameter of the tumor in millimeters (mm) in the superior-inferior (SI), lateral-medial (LM) and anterior-posterior (AP) planes by 0.523 as the correction factor [SI x LM x AP x 0.523].

Angiography—Angiography was performed in 3 non-tumor bearing rats and 1 tumor-bearing rat to determine procedure feasibility and safety using a SIREMOBIL Compact digital C-Arm (Siemens Healthcare, Malvern, PA). Rats were shaved and prepped in a sterile manner. Under the operating microscope, a femoral cutdown was performed and the femoral artery isolated. A 22 gauge intravenous (I.V.) catheter was inserted into the femoral artery. The rat was transferred to the angiography suite. A Mirage™ 0.008 inch (0.20mm) hydrophilic guidewire (Micro Therapeutics Inc., Irvine, CA) was advanced into the abdominal aorta. A 1.5F Marathon Flow Directed Micro Catheter (Micro Therapeutics Inc., Irvine, CA) was advanced over the guidewire. Omnipaque™ iodinated contrast material (300mgI/ml) was diluted by 50% in normal saline and 1–2 ml was used per injection (GE Healthcare Inc, Princeton, NJ). Aortogram was performed to locate the celiac trunk followed by selective celiac and hepatic arteriograms.

Clinical and Laboratory Assessment

Rats were weighed at baseline and weekly thereafter as well as monitored daily. In addition, 0.15 ml of blood was drawn from the tail vein at baseline and 7-days post surgery to biochemically monitor liver dysfunction in 4 CBDL and 4 SBDL rats. Three 400–450g normal control rats underwent baseline blood draws. All blood samples were run on the VetScan VS2® Blood Laboratory System (Abaxis, Union City, CA) using the Comprehensive Diagnostic Profile rotor.

MR-guided laser ablation

All laser ablation experiments were performed using an FDA approved 980-nm laser generator with a maximal power setting of 15W (Visualase, Houston, Texas). Four rats were anesthetized and prepped as described above. A bare 400μm core optical laser fiber with a 1.0-cm diffusing tip was inserted into the middle hepatic lobe through a 22-gauge introducer needle under intermittent MR imaging. Pre-ablation imaging as outlined above consisted of T1- and T2-FSE images. Intraprocedural imaging was performed continuously in the axial plane with gradient echo (GRE) imaging giving magnitude and phase images. The liver was ablated at a power setting of 3 watts for 2 minutes. Post-ablation MR imaging was performed as described above with T1- and T2-FSE imaging. Rats were euthanized using CO_2 inhalation immediately (N=1), 90 minutes (N=1) and 24 hours (N=2) post-ablation and the liver tissue harvested for gross and microscopic pathologic analysis to assess early temporal changes in the ablated tissue.

Pathology

All rats were euthanized using CO_2 inhalation 7-days post surgery except one control tumor bearing rat that was followed for 3 weeks post cell injection. The liver and tumor tissue were harvested for gross and microscopic analysis from all hepatic lobes in all rats. In addition, lung tissue was harvested from rats from each ligation group to examine for metastases. The specimens were placed in 10% neutral buffered formalin (Fisher Scientific/Acros, Waltham, MA), embedded in paraffin, sectioned with a microtome and stained with hematoxylin-eosin (H&E) and Mason's Trichome stain to outline the hepatic architecture. Slides from all hepatic lobes were evaluated for tumor growth, invasion, necrosis and cytologic features. The background liver parenchyma and biliary structures were also evaluated for fibrosis, hyperplasia and patency of the portal tracts and microvasculature. All slides were evaluated by light microscopy by an experienced pathologist (20 years) blinded to the study group allocation.

Statistical Analysis

Statistical analyses were performed using SAS Version 9.2 (SAS Institute, Cary, NC). Tumor volumes (mm^3) were analyzed using the Kruskall-Wallis test followed by post-hoc pair-wise comparison between tumors in the normal (control)/SBDL non-ligated, SBDL ligated lobe and CBDL groups using the exact Mann-Whitney test. For analysis of clinical and laboratory parameters, baseline values between the SBDL and CBDL were assessed using the student's t-test (or Mann-Whitney test). To test for within group clinical and laboratory parameter differences, the mean difference ± SD for each value from baseline to follow-up for each animal in SBDL and CBDL groups was calculated and the mean difference assessed using the student's t-test (or exact Mann-Whitney test). Within group differences from baseline to follow-up for any laboratory parameters determined significant were compared between the SBDL and CBDL groups using the Mann Whitney test. The level for statistical significance was set at $p<0.05$.

RESULTS

MRI

3.0T MR imaging demonstrated hyperintense T2-weighted (Figure 2a, 2c, 3a, 3c) and hypointense T1-weighted (Figure 2b, 2d, 3b, 3d) liver lesions in the control (normal liver) (Figure 2a, b), CBDL (Figure 2c, d), SBDL ligated lobe (Figure 3a,b) and SBDL non-ligated lobe (Figure 3c, d) rats, respectively. **Tumor Induction:** MR imaging revealed solitary liver lesions at 5/10 (50.0%) sites in normal control rats, 7/8 (87.5%) sites in SBDL and 12/12 (100%) sites in CBDL rats. Further subdividing the SBDL group, tumors were seen in 4/4 sites in the ligated lobes and 3/4 sites in the non-ligated lobes. In one normal control liver rat, a 5–6mm tumor was visualized by MR imaging at 7 days post injection but no longer evident by 21 days. **Tumor Size:** The median (range) tumor volume was 63.6 mm^3 (1.8–286.2 mm^3) in the control (normal) and SBDL non-ligated lobe, 387.1 mm^3 (205.8–543.9 mm^3) in SBDL ligated lobe and 149.5 mm^3 (52.6–618.3 mm^3) in CBDL rats. Overall, the median tumor volume differed significantly by group ($p<0.02$). The median tumor volume was significantly larger in both the SBDL and CBDL groups compared to the normal/non-ligated SBDL group ($p<0.02$ and $p<0.03$ respectively) but there was no significant difference in tumor volume between the SBDL ligated and CBDL groups ($p=0.3$). Furthermore, in the SBDL rats, the tumor volumes were significantly larger in the ligated lobe compared to the non-ligated lobe ($p=0.03$). **Biliary System:** MR imaging revealed a dilated common bile duct in CBDL rats (Figure 2c,d, arrowheads) and evidence of intrahepatic bile duct dilation in both the CBDL and ligated lobe of SBDL rats.

Angiography

Angiography was well tolerated and successfully completed in all 4 rats undergoing the procedure. Aortogram (Figure 4a) and selective celiac arteriogram (Figure 4b) demonstrated renal, mesenteric and hepatic arterial anatomy. Angiography of the tumor-bearing rat revealed an enhancing tumor stain in the middle hepatic lobe following contrast injection (Figure 4c) that corresponded with the location and enhancement pattern (Figure 4d) seen by gadolinium-enhanced FSE T1 MRI.

Clinical and Laboratory Assessment—On physical exam, CBDL rats demonstrated decreased alertness and increased somnolence as well as ascites by postoperative day (POD) 7. In contrast, SBDL and control rats demonstrated normal level of alertness and no evidence of ascites. CBDL rats lost an average of 69.5 ± 10.3 grams ($p = 0.01$) or approximately 17% of their body weight by 7 days. However, given the presence of ascites, the percentage of body weight loss and degree of decompensation may be underestimated. In contrast, SBDL rats maintained their weight with an average loss of only 0.25 ± 1.7 grams ($p = 0.89$). The difference in weight from baseline to follow-up for the CBDL group compared to the SBDL group was significant ($p=0.03$).

Baseline and follow-up laboratory values are summarized in Table 1 as mean ± SD. There was no significant difference in any of the laboratory parameters at baseline between the SBDL and CBDL groups. Laboratory analysis revealed a significant increase in serum total bilirubin (7.5 ± 3.3 mg/dl; $p = 0.02$) and a decrease in albumin (−2.1 ± 0.7 g/dl; $p<0.01$) levels in CBDL rats from baseline to follow-up but no change in SBDL rats ($p= 1.0$ for both) from baseline. In contrast, none of the laboratory parameters were significantly different in the SBDL group from baseline to follow-up. Moreover, there was a significant difference in the change in total bilirubin and albumin from baseline to follow-up in the CBDL group compared to the SBDL group ($p=0.03$).

Pathology—Samples were assessed from all rats and representative images are shown in Figure 5. Gross pathologic analysis of the liver and tumor revealed a firm, dense yellow colored mass growing within the liver parenchyma in tumor bearing rats (Figure 5a). There was evidence of local extension of N1S1 tumor to the omentum in CBDL rats but none of the other groups. Examination of the abdominal cavity revealed evidence of large volume ascities and yellowing of the connective tissue in CBDL but not in SBDL or control rats. Maintenance of bile duct ligation was confirmed in all ligation animals.

H&E analysis revealed a high-grade liver tumor with evidence of nuclear atypia, mitotic figures (Figure 5b) and minimal areas of central tumor necrosis. In addition, analysis of tumor and liver tissue from CBDL rats revealed an expansive tumor with significant bile duct hyperplasia and local invasion (Figure 5c). Trichrome stain revealed early moderate-severe bridging fibrosis of the background liver parenchyma in CBDL rats (Figure 5d). In addition, there was evidence of significant periductular, bridging and intratumoral fibrosis as well as development of a fibrous pseudocapsule at the margin of the tumor-liver interface (Figure 5e). Lastly, tumor thrombi were identified in dilated branches of the portal vein (Figure 5f).

H&E and trichrome analysis of tissue from the SBDL rats revealed significant intratumoral and pseudocapsular fibrosis at the tumor-liver margin in tumors from both the ligated lobe (Figure 5g) and non-ligated lobe (Figure 5h). However, there was evidence of bile duct hyperplasia, mild-moderate periductular and parenchymal fibrosis and greater local tumor extension in the ligated lobe (Figure 5g) compared to the non-ligated tumor bearing lobes within the same animal. Tumor tissue from one control (non-ligated) rat revealed tumor growth with intratumoral fibrosis similar to the SBDL non-ligated lobe (data not shown). Moreover, histologic analysis of tissue from SBDL non-ligated, non-tumor bearing hepatic lobes and control rat livers did not reveal any evidence of tumor metastasis, bile duct hyperplasia, hepatocyte necrosis or fibrosis while the portal tracts and microvasculature were patent (Figure 5g). Finally, lung sections were analyzed from several tumor-bearing rats but did not reveal evidence of distant metastases by 7–10 days post inoculation (data not shown).

MR-guided Laser Ablation—4 non-tumor bearing rats underwent MR-guided laser ablation to test the feasibility and safety of the procedure. All rats tolerated the procedure well and there was no evidence of burning of the skin, abdominal wall or other abdominal organs. Pre-ablation imaging located the laser fiber in the axial plane (Figure 6a, arrowheads). Respiration motion limited the image quality of the intraprocedural phase images and warrants further refinement. Post ablation FSE T2 imaging demonstrated increased T2 signal within a 1–2 cm ablation zone contained within the liver (Figure 6b). Pre-gadolinium FSE T1 imaging demonstrated high T1 signal within the ablation zone (not shown) and a lack of enhancement throughout the ablation zone (Figure 6c). Gross pathologic analysis of the ablated liver immediately post-procedure demonstrated a centrally white zone of ablation while examination at 90 minutes and 24 hours after the ablation demonstrated a centrally white ablation zone with a peripheral "red zone" or hyperemic rim(16) (Figure 6d). Histologic analysis of H&E stained sections of the ablated tissue immediately post-ablation demonstrated features of reversible and irreversible hepatocyte injury in different regions of the ablative zone including edema, hemorrhage, microvesicular steatosis, fragmentation of the endothelial cells lining the sinusoids and biliary epithelium and features suggestive of early coagulative necrosis (Figure 6e). Analysis of H&E stained sections of the ablated tissue 90 minutes after the ablation revealed evidence of further irreversible hepatocyte injury and more extensive hemorrhage, particularly at the ablative margin demarcating the area of injured liver tissue and normal background parenchyma (Figure 6f). Finally, morphologic assessment at 24 hours post-ablation revealed evidence of a central zone of early coagulative necrosis (data not shown). However, morphologic assessment at the all time points revealed areas of indeterminate injury and necrosis, particularly at the ablation margin, suggesting that thermal fixation of the tissue may be present and that vital stains or molecular markers would be necessary in order to fully assess tissue response to injury (16, 17).

DISCUSSION

In this study a rat hepatocellular carcinoma disease model was successfully developed and utilized for MR imaging and preliminary interventional oncologic applications. This represents a multifunctional animal model of HCC where pre-clinical studies can proceed from *in vitro* to *in vivo* animal model suitable for testing image-guided percutaneous and catheter directed ablation therapies.

HCC is representative of the current limitations for animal models in the field of interventional oncology (1, 2). Although HCC is one of the most widely studied tumors clinically in the field of interventional oncology, pre-clinical studies of the thermal biology and molecular mechanisms of HCC resistance and recurrence following percutaneous- and catheter directed therapies have been limited owing to the lack of biologically relevant animal models. Most importantly, no model has recapitulated the unique disease model of HCC comprising both liver dysfunction and malignancy, critical modifiers of hepatocarcinogenesis and tumor progression. Previous studies in rat liver tumor models have demonstrated the technical aspects and feasibility of model development, imaging and extension to interventional oncologic investigations as well as histologic characterization of different models (5, 6, 8, 18, 19). Despite growing interest and promise in the use of orthotopic rat liver tumor models in the field of interventional oncology and oncologic liver imaging, existing rat liver tumor models have not addressed all the key issues of biological and clinical relevance critical for a translational HCC model (2). This study aimed to build on the recent work by Ju et al. and Guo et al. (5, 6) by introducing bile duct ligation methods into the N1S1 HCC model as a method to generate background liver fibrosis.

There are several advantages of this tumor model. First, the CBDL and SBDL models demonstrated reliable tumor induction with development of clinically relevant tumor sizes within 7 days. In addition, given the rapid tumor induction, animal housing and maintenance costs were minimized and thus the model is relatively inexpensive to generate and utilize. The model is compatible with conventional clinical imaging systems and ablative devices. Finally, the rat HCC model was developed with 3 distinct physiologic sub-types via implantation of tumor cells combined with varying degrees of bile duct ligation resulting in a spectrum of cholestatic-induced liver fibrosis and dysfunction.

Second, this model is more biologically relevant to human HCC. The model combines a syngeneic HCC cell line and liver injury in an immune competent rat to generate a liver cancer disease model. An immune competent model is important because immune surveillance and recognition, particularly Kupffer cell activity in the liver, plays a critical role in hepatic tumorigenesis (13). Of note, one of the tumors in a control rat regressed by 3 weeks, suggesting that the local tumor microenvironment may play a critical role in immune response and tumor surveillance. In addition, the N1S1 cell line is easily propagated in cell culture and therefore can be studied using cellular, molecular and genomic techniques in parallel to the animal model. Although the rat N1S1 HCC tumor model in the setting of a normal liver background provided a useful model for developing imaging and ablation techniques, this model does not recapitulate HCC in the setting of background liver disease. As such, the CBDL and SBDL models were developed to improve the biological relevance of the model.

The CBDL and SBDL models recapitulate a more biologically, histologically and clinically relevant model of HCC as evidenced by the liver metabolic and synthetic dysfunction (CBDL only) as well as tumor progression in the presence of developing liver fibrosis. The CBDL model may be more feasible for shorter-term studies examining percutaneous ablative techniques as well as mechanistic studies into the role of the tumor microenvironment on the pathogenesis of HCC. On the other hand, the SBDL model with segmental ligation affords reliable tumor induction in an animal that will suffer less than the CBDL rats and may be more feasible for longer-term survival studies examining both percutaneous and catheter-directed interventional oncologic therapies as well as systemic delivery of anti-cancer drugs for pre-clinical testing of antitumor activity. The SBDL model with multiple tumors in different microenvironments within the same animal affords a unique opportunity to examine the relative importance of local tumor microenvironment on both mechanisms of tumorigenesis and therapeutic response but results should be interpreted carefully and relative to appropriate control tumors.

Finally, the model is compatible with clinical imaging systems including MR and angiography as well as percutaneous MR-guided laser ablation (20, 21). In this pilot study, percutaneous MR-guided laser ablation of the liver was safe and feasible (Figure 6). Extension of MR-guided laser ablation to the tumor model for studies examining therapeutic efficacy will be the subject of future investigation. Guo et al. demonstrated the feasibility of studying irreversible electroporation (IRE) in the N1S1 model in the absence real-time image-guidance (8). MR-guided laser ablation offers the advantage that it can be performed in the rat model with near real-time treatment monitoring in a similar manner to the clinical setting but further refinement of the intraprocedural phase imaging is warranted. Importantly, the model may facilitate histologic and molecular assessment of the treatment effects of thermal ablation (17, 22).

Nonetheless, the model outlined has several limitations. First, although 400–450g rats were used in this study, the rats are still relatively small compared to larger rabbit VX-2 tumor or porcine models used in interventional oncology. Nevertheless, imaging and percutaneous thermal ablation were technically feasible, safe and provided high-resolution images using clinical equipment. Second, orthotopic tumors do not represent *de novo* tumors that develop spontaneously in patients with HCC. Moreover, although the bile duct ligation methods outlined resulted in a spectrum of liver fibrosis and dysfunction, bile duct ligation does not represent one of the common etiologies underlying liver disease in human HCC, such as chronic Hepatitis B or C viral infection or alcoholic cirrhosis (23). Previous studies have used chemical carcinogenesis including chronic dinitroethylomaine (DEN) exposure to induce liver disease and HCC tumorigenesis in rats (24). Although this method is effective at generating primary liver cancer in the background of liver disease, it is labor intensive, expensive, takes 3–4 months to develop and results in multifocal disease. Thus, although the model presented here neither represents *de novo* hepatocarcinogenesis nor recapitulates true cirrhosis, the orthotopic ligation model is a potentially useful alternative that allows reliable development of discrete tumors in the setting of background liver fibrosis and dysfunction and thus may be more ideal for local-regional interventional oncologic investigations studying clinically relevant questions (25, 26). Finally, emerging whole gene expression studies in human HCC have identified different molecular sub-types for HCC with different prognoses and therapeutic responses (27–30). The N1S1 cell line used in this model requires further genetic and molecular characterization in order to phenotype this model relative to human HCC and warrants further examination in a larger sample size of rats. Of note, extension of the orthotopic ligation methods outline here to the recently described Buffalo rat Morris hepatoma model warrants further investigation, especially given the evidence for greater metastatic potential in the Morris over the N1S1 model (5).

Minimally invasive, image-guided percutaneous and catheter-directed therapies have emerged as critical therapies in the multidisciplinary treatment of patients with HCC (31, 32). The growing field of interventional oncology is well positioned to utilize recent advancements in genomics, molecular biology, anti-cancer therapeutics and drug delivery (31). The model outlined may serve as a biologically relevant, translational model of HCC that may be utilized for pre-clinical studies testing interventional oncologic percutaneous and catheter-directed therapies as well as mechanistic studies of the role of the tumor microenvironment in resistance to interventional oncologic therapies and the pathogenesis of HCC. The long-term goal is to utilize the model to advance the science and accelerate the translation of image-guided interventional oncologic therapies for patients with HCC.

Acknowledgments

Funding Information

Infrastructure support provided by NIH construction grant NIH C06 RR018898 and Center for Translational Science Activities (CTSA) grant NIH UL1 RR024150. Research support provided in part by SIR Foundation Allied Scientist Training Grant (Mr. Scott Thompson) and RSNA Research Scholar Grant (Dr. David Woodrum).

References

1. Aravalli RN, Golzarian J, Cressman EN. Animal models of cancer in interventional radiology. Eur Radiol. 2009; 19:1049–1053. [PubMed: 19137307]
2. Aravalli RN, Steer CJ, Sahin MB, Cressman EN. Stem cell origins and animal models of hepatocellular carcinoma. Dig Dis Sci. 2010; 55:1241–1250. [PubMed: 19513833]
3. Li X, Zhou X, Guan Y, Wang YX, Scutt D, Gong QY. N-nitrosodiethylamine-induced pig liver hepatocellular carcinoma model: radiological and histopathological studies. Cardiovasc Intervent Radiol. 2006; 29:420–428. [PubMed: 16502159]
4. Yang W, Ahmed M, Elian M, et al. Do liposomal apoptotic enhancers increase tumor coagulation and end-point survival in percutaneous radiofrequency ablation of tumors in a rat tumor model? Radiology. 2010; 257:685–696. [PubMed: 20858851]
5. Guo Y, Klein R, Omary RA, Yang GY, Larson AC. Highly malignant intra-hepatic metastatic hepatocellular carcinoma in rats. Am J Transl Res. 2010; 3:114–120. [PubMed: 21139811]
6. Ju S, McLennan G, Bennett SL, et al. Technical aspects of imaging and transfemoral arterial treatment of N1-S1 tumors in rats: an appropriate model to test the biology and therapeutic response to transarterial treatments of liver cancers. J Vasc Interv Radiol. 2009; 20:410–414. [PubMed: 19167243]

7. Lin WY, Tsai SC, Hsieh JF, Wang SJ. Effects of 90Y-microspheres on liver tumors: comparison of intratumoral injection method and intra-arterial injection method. J Nucl Med. 2000; 41:1892–1897. [PubMed: 11079501]
8. Guo Y, Zhang Y, Klein R, et al. Irreversible electroporation therapy in the liver: longitudinal efficacy studies in a rat model of hepatocellular carcinoma. Cancer Res. 2010; 70:1555–1563. [PubMed: 20124486]
9. Chan HH, Chu TH, Chien HF, et al. Rapid induction of orthotopic hepatocellular carcinoma in immune-competent rats by non-invasive ultrasound-guided cells implantation. BMC Gastroenterol. 2010; 10:83. [PubMed: 20649994]
10. Yang JD, Kim WR, Coelho R, et al. Cirrhosis is present in most patients with hepatitis B and hepatocellular carcinoma. Clin Gastroenterol Hepatol. 2011; 9:64–70. [PubMed: 20831903]
11. Yang JD, Nakamura I, Roberts LR. The tumor microenvironment in hepatocellular carcinoma: Current status and therapeutic targets. Semin Cancer Biol. 2011; 21:35–43. [PubMed: 20946957]
12. Chen WY, Chen CJ, Liao JW, Mao FC. Chromium attenuates hepatic damage in a rat model of chronic cholestasis. Life Sci. 2009; 84:606–614. [PubMed: 19302800]
13. Tsujimoto T, Kuriyama S, Yamazaki M, et al. Augmented hepatocellular carcinoma progression and depressed Kupffer cell activity in rat cirrhotic livers. Int J Oncol. 2001; 18:41–47. [PubMed: 11115537]
14. Mayrhauser U, Stiegler P, Stadlbauer V, et al. Effect of hyperthermia on liver cell lines: important findings for thermal therapy in hepatocellular carcinoma. Anticancer Res. 2011; 31:1583–1588. [PubMed: 21617213]
15. Aller, MA.; Arias, JL.; Prieto, I.; Arias, J. [Accessed 1 October 2010.] A suitable microsurgical method for obstructive cholestasis in the rat. Nature Protocol Exchange. 2010. Available at: http://www.nature.com/protocolexchange/protocols/647/uploads/1411
16. Goldberg SN, Grassi CJ, Cardella JF, et al. Image-guided tumor ablation: standardization of terminology and reporting criteria. J Vasc Interv Radiol. 2009; 20:S377–390. [PubMed: 19560026]
17. Cho YK, Kim Y, Rhim H. Pitfalls in the radiological and pathological correlation of tumour response rates of hepatocellular carcinoma following radiofrequency ablation. J Clin Pathol. 2009; 62:1071–1073. [PubMed: 19946093]
18. Li X, Zheng CS, Feng GS, Zhuo CK, Zhao JG, Liu X. An implantable rat liver tumor model for experimental transarterial chemoembolization therapy and its imaging features. World J Gastroenterol. 2002; 8:1035–1039. [PubMed: 12439920]
19. Chen F, Sun X, De Keyzer F, et al. Liver tumor model with implanted rhabdomyosarcoma in rats: MR imaging, microangiography, and histopathologic analysis. Radiology. 2006; 239:554–562. [PubMed: 16543589]
20. Stafford RJ, Fuentes D, Elliott AA, Weinberg JS, Ahrar K. Laser-induced thermal therapy for tumor ablation. Crit Rev Biomed Eng. 2010; 38:79–100. [PubMed: 21175405]
21. Gough-Palmer AL, Gedroyc WM. Laser ablation of hepatocellular carcinoma--a review. World J Gastroenterol. 2008; 14:7170–7174. [PubMed: 19084930]
22. Sofocleous CT, Nascimento RG, Petrovic LM, et al. Histopathologic and immunohistochemical features of tissue adherent to multitined electrodes after RF ablation of liver malignancies can help predict local tumor progression: initial results. Radiology. 2008; 249:364–374. [PubMed: 18796687]
23. Yang JD, Roberts LR. Epidemiology and management of hepatocellular carcinoma. Infect Dis Clin North Am. 2010; 24:899–919. viii. [PubMed: 20937457]
24. Wang J, Zhang S, Li Z, et al. (1)H-NMR-based metabolomics of tumor tissue for the metabolic characterization of rat hepatocellular carcinoma formation and metastasis. Tumour Biol. 2011; 32:223–231. [PubMed: 20890798]
25. Mertens JC, Martin IV, Schmitt J, et al. Multikinase inhibitor sorafenib transiently promotes necrosis after radiofrequency ablation in rat liver but activates growth signals. Eur J Radiol. 2011
26. Hoffmann K, Glimm H, Radeleff B, et al. Prospective, randomized, double-blind, multi-center, Phase III clinical study on transarterial chemoembolization (TACE) combined with Sorafenib

versus TACE plus placebo in patients with hepatocellular cancer before liver transplantation - HeiLivCa [ISRCTN24081794]. BMC Cancer. 2008; 8:349. [PubMed: 19036146]

27. Lee JS, Chu IS, Mikaelyan A, et al. Application of comparative functional genomics to identify best-fit mouse models to study human cancer. Nat Genet. 2004; 36:1306–1311. [PubMed: 15565109]
28. Lee JS, Thorgeirsson SS. Comparative and integrative functional genomics of HCC. Oncogene. 2006; 25:3801–3809. [PubMed: 16799621]
29. Andersen JB, Factor VM, Marquardt JU, et al. An integrated genomic and epigenomic approach predicts therapeutic response to zebularine in human liver cancer. Sci Transl Med. 2010; 2:54ra77.
30. Chi JT, Thrall DE, Jiang C, et al. Comparison of genomics and functional imaging from canine sarcomas treated with thermoradiotherapy predicts therapeutic response and identifies combination therapeutics. Clin Cancer Res. 2011; 17:2549–2560. [PubMed: 21292819]
31. Becker GJ. Interventional oncology: perspectives on current scholarly productivity and potential for future growth. Radiology. 2010; 257:309–312. [PubMed: 20959543]
32. Lewandowski RJ, Geschwind JF, Liapi E, Salem R. Transcatheter intraarterial therapies: rationale and overview. Radiology. 2011; 259:641–657. [PubMed: 21602502]

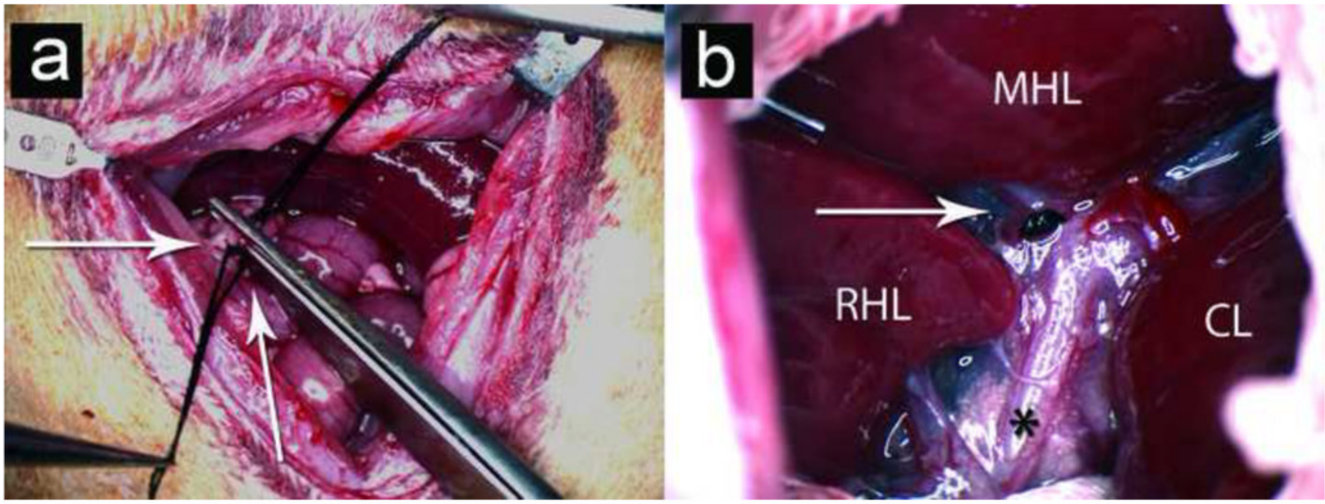

Figure 1.

Creation of an orthotopic, liver injury tumor model with bile duct ligation and N1S1 cell injection. **(a)** Common bile duct ligation (CBDL): CBD is triply tied and cut (white arrows). **(b)** Selective Bile Duct Ligation (SBDL): Ligation of biliary branch to the middle hepatic lobe is with black nylon suture (white arrow); (*) denotes common bile duct. Key: RHL = Right Hepatic Lobe; MHL = Middle Hepatic Lobe; CL = Caudate Lobe.

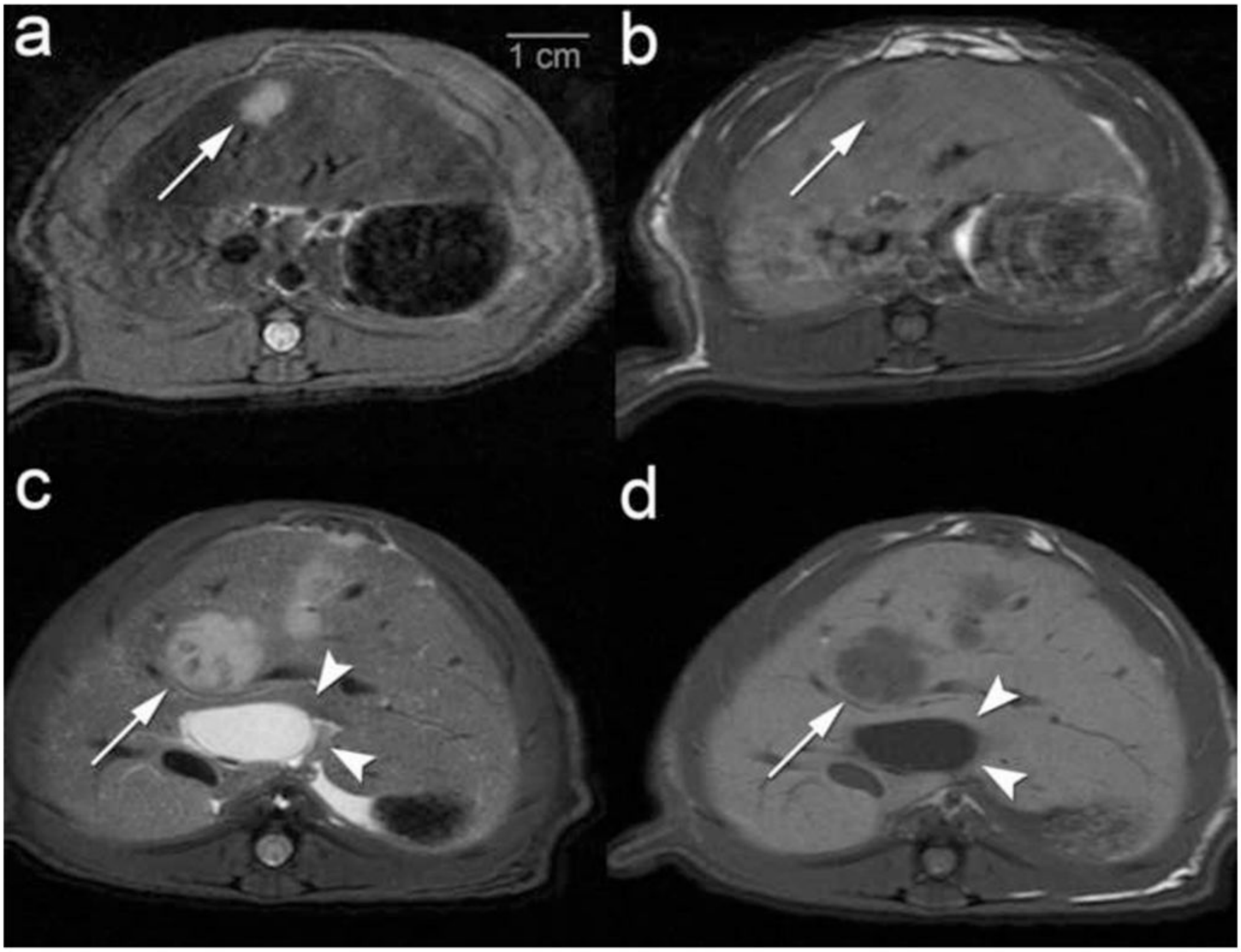

Figure 2.
3.0T Axial MR imaging of non-ligated (control) and common bile duct ligation (CBDL) tumor model 7–10 days post surgery with cell injection at the time of surgery. MR images demonstrate hyperintense liver lesions on Fast Spin Echo (FSE) T2 and hypointense liver lesions of FSE T1. **(a, b)** Control rat with a 0.5 cm tumor in middle hepatic lobe (white arrows) with **(a)** FSE T2 and **(b)** FSE T1 imaging. **(c, d)** CBDL rat with a 1.2 cm tumor in middle hepatic lobe (white arrows) and evidence of a dilated common bile duct (white arrowheads) with **(c)** FSE T2 and **(d)** FSE T1 imaging.

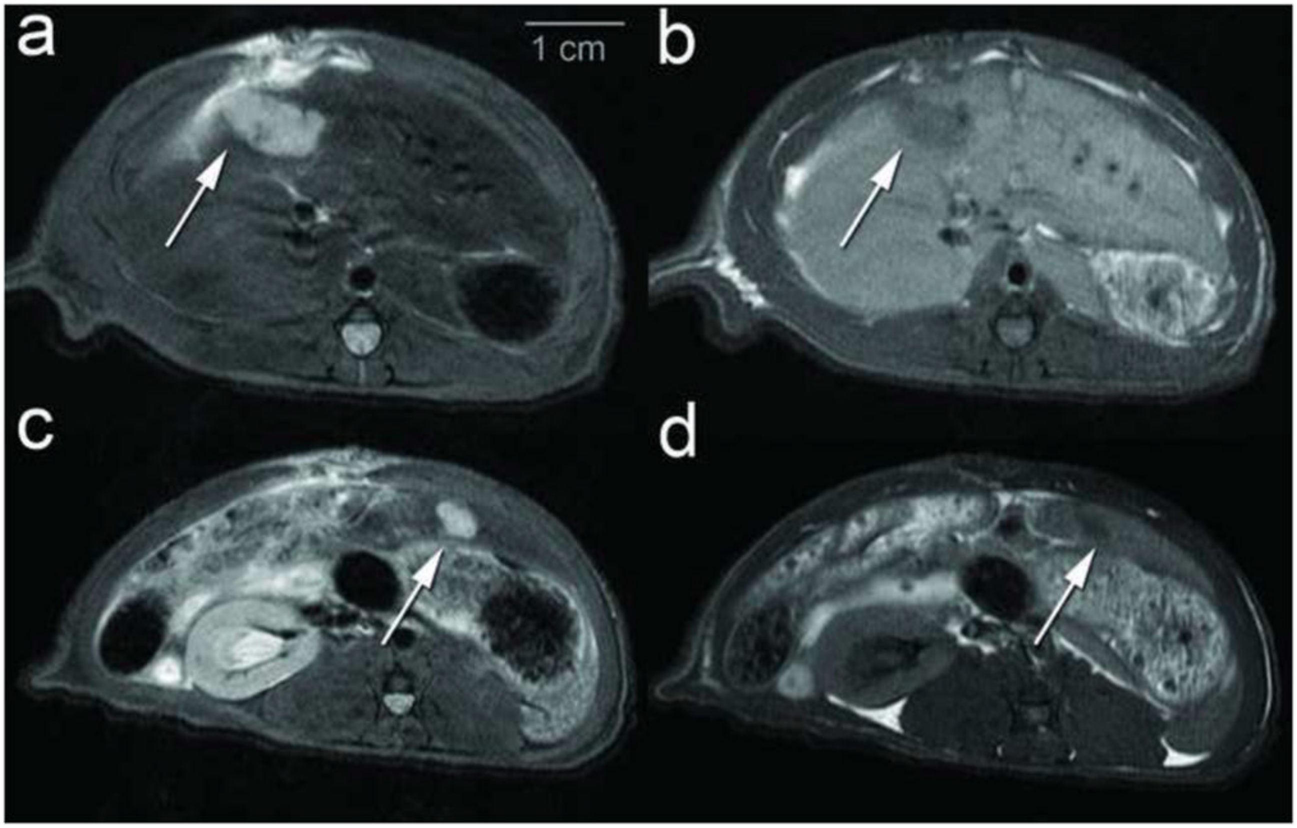

Figure 3.
3.0T Axial MR imaging of Selective Bile Duct Ligation (SBDL) rat examining the non-ligated and ligated hepatic lobes and tumor growth differences 7–10 days post surgery with cell injection at the time of surgery. MR images demonstrate hyperintense liver lesions on Fast Spin Echo (FSE) T2 and hypointense liver lesions of FSE T1. **(a, b))** SBDL rat with a 1.1 cm tumor in the ligated middle hepatic lobe (MHL) (white arrow) with **(a)** FSE T2 and **(b)** FSET1 imaging. **(c, d)** Same SBDL rat with a 0.5 cm tumor in the non-ligated left lateral hepatic lobe (white arrow) with **(c)** FSE T2 and **(d)** FSE T1 imaging.

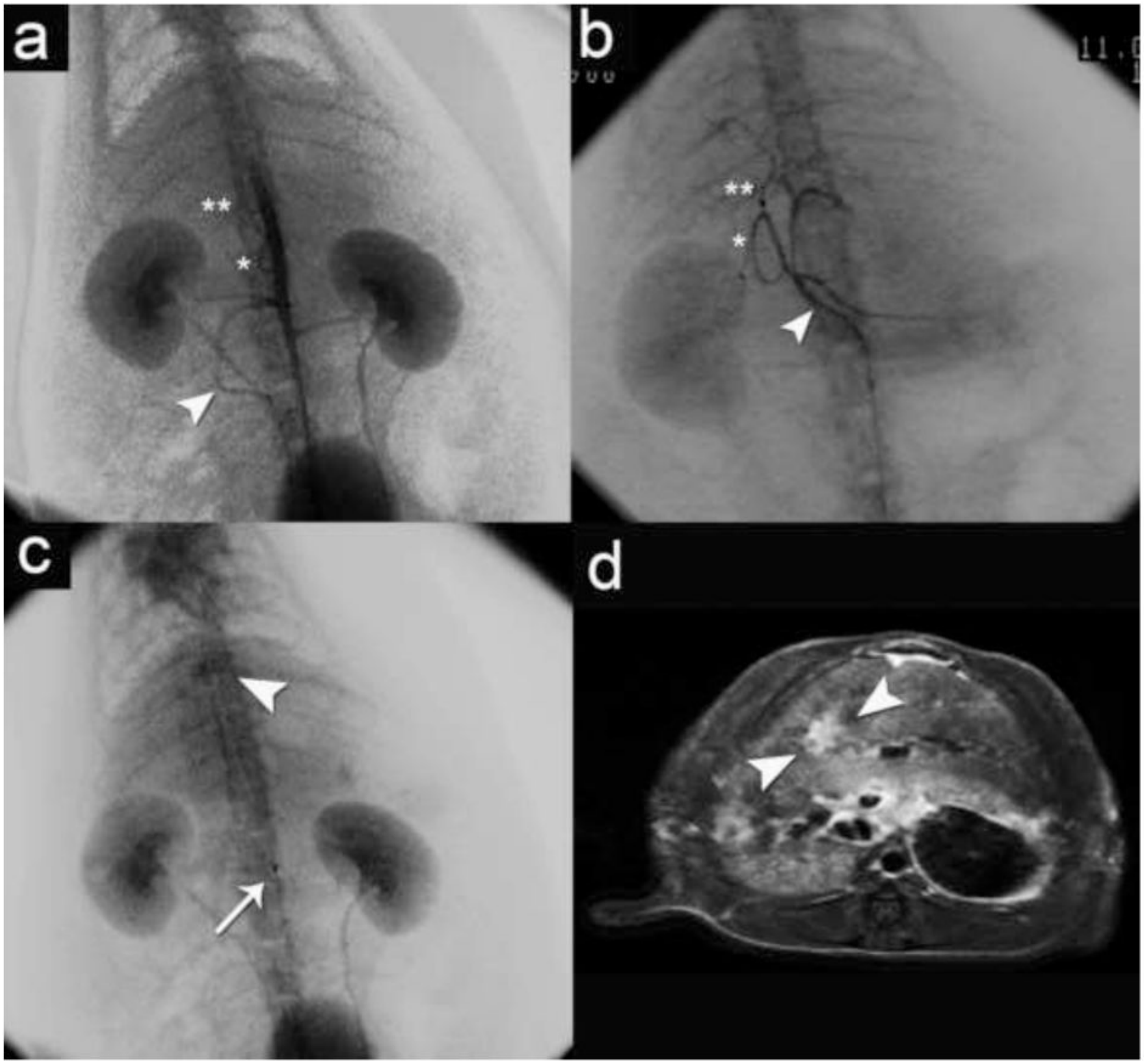

Figure 4.

Angiography with corresponding post-gadolinium enhanced Fast Spin Echo (FSE) T1 MR images**. (a)** Aortogram demonstrating renal and mesenteric arterial anatomy superior mesenteric artery (white arrowhead), celiac trunk (*) and proper hepatic artery (**) **(b)** Selective celiac arteriogram demonstrating the primary arterial branching of the celiac artery (white arrowhead) to the spleen, pancreas, stomach and liver including gastroduodenal artery (*) and common and proper hepatic artery (**); **(c)** Selective hepatic arteriogram demonstrating a differential tumor stain (white arrowhead) in the liver (catheter tip denoted by white arrow) **(d)** Post-gadolinium axial FSE T1 demonstrates tumor enhancement (white arrowheads) corresponding to tumor stain in **(d)**.

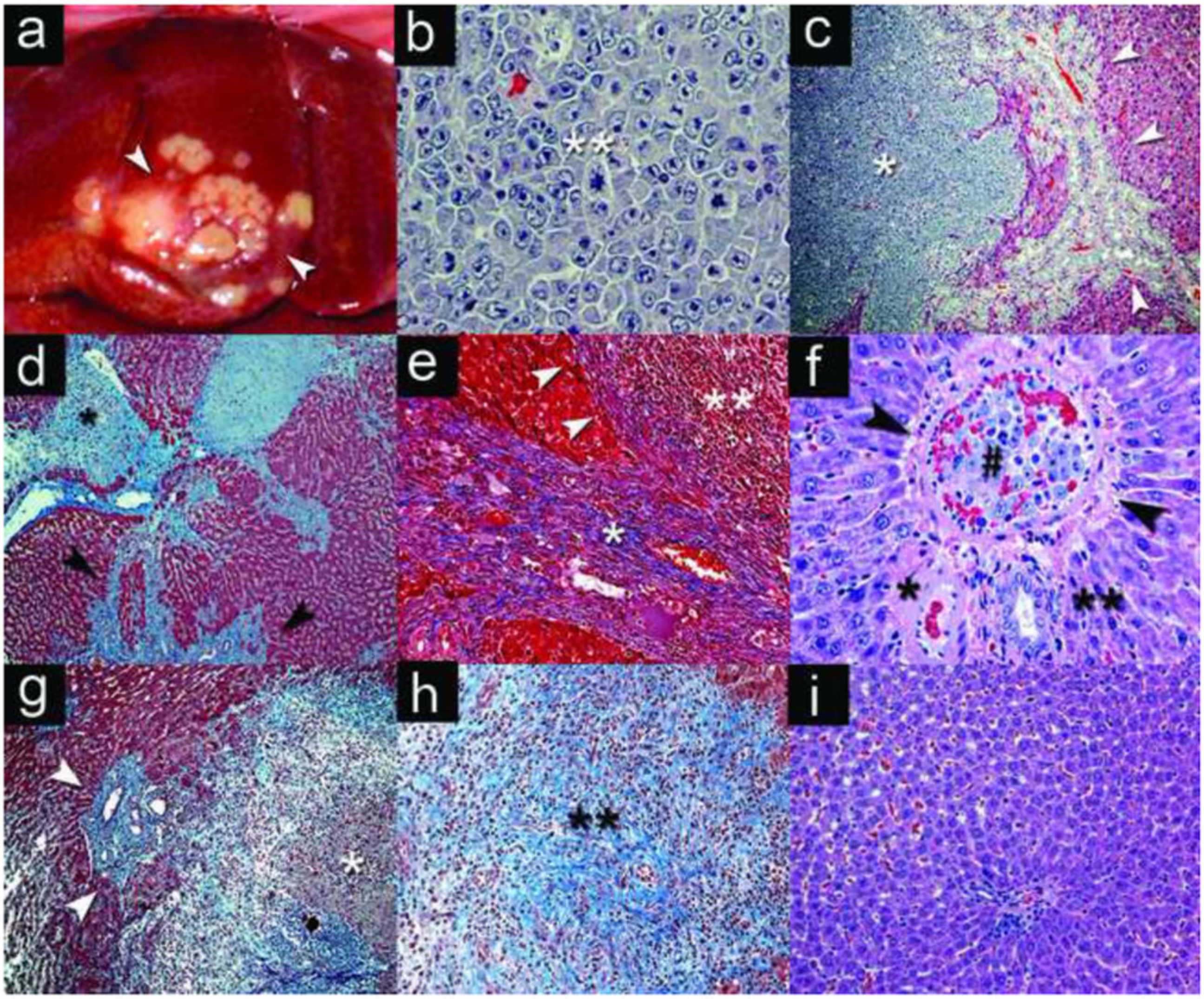

Figure 5.

Gross and microscopic pathology of N1S1 tumor model. **(a)** Gross pathology of N1S1 tumor in the middle hepatic lobe (white arrowheads) of a CBDL rat 7 days post surgery with cell injection at the time of surgery. Photomicrographs: **(b)** N1S1 tumor cells from CBDL rat with evidence of pleiomorphism, large hyperchromatic and atypial nuclei with mitotic figures (**)) (H&E 400x). **(c)** N1S1 tumor (*) and bile duct hyperplasia (white arrowheads) in CBDL rat (H&E, 40x). **(d)** N1S1 satellite tumor (*) with moderate-severe bridging and periductular fibrosis (black arrowheads) in CBDL rat (Trichrome stain, 40x). **(e)** Severe fibrosis (*) with pseudocapsule (white arrowheads) around tumor margin (**) (Trichrome 100x). **(f)** Tumor thrombus (#) in branch of the portal vein (PV) (black arrowheads) with patent branch of the hepatic artery (*) and bile duct (**) in CBDL rat (H&E 200x). **(g)** SBDL ligated-lobe of tumor (*) with intratumoral, peritumoral and periductular fibrosis (blue) with bile duct hyperplasia (white arrowheads) (Trichrome 40x). **(h)** SBDL non-ligated lobe with early intratumoral fibrosis (**) (Trichrome 40x); I) Normal liver tissue from SBDL non-ligated, non-tumor bearing lobe (H&E 200x).

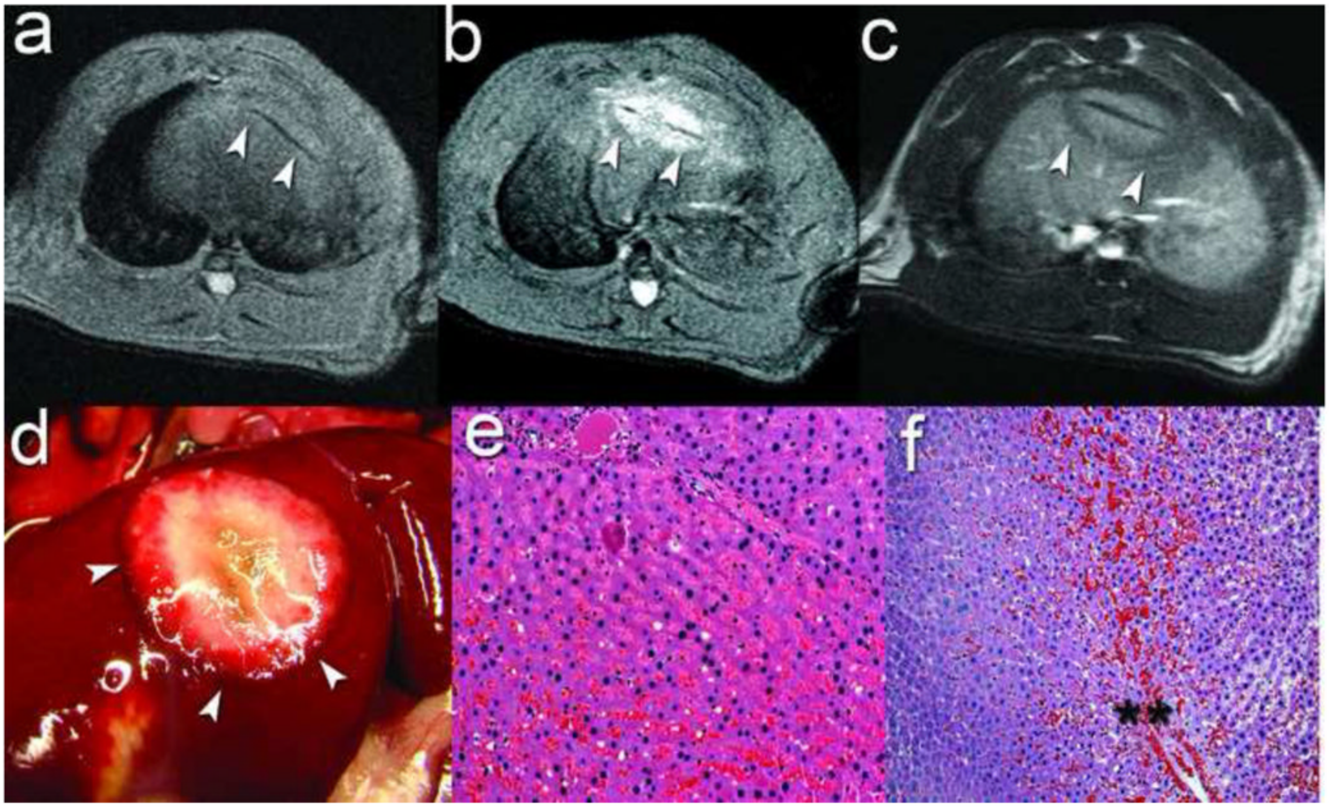

Figure 6.

Percutaneous MR-guided laser ablation. **(a)** Pre-ablation Axial FSE T2 for laser fiber localization (white arrowheads) in the middle hepatic lobe (MHL). **(b)** Post-ablation axial FSE T2 demonstrating increased T2 signal within the ablation zone (white arrowheads) **(c)** Post-ablation gadolinium-enhanced axial FSE T1 demonstrating a central zone of increased T1 signal with a lack of enhancement in the ablation zone (white arrowheads). **(d)** Gross pathology of liver 90 minutes post-ablation demonstrating a centrally white ablative zone with hemorrhage at the ablation margin (white arrowheads). Photomicrographs: **(e)** Microsocopic analysis of the central white zone immediately post-ablation demonstrating features of reversible and irreversible hepatocyte injury and thermal fixation (H&E, 100x); **(f)** Microscopic analysis 90 minutes post-ablation of the ablation margin demonstrating the hemorrhagic margin (**) between the adjacent background liver parenchyma on the left and the injured liver tissue within the zone of ablation on the right (H&E, 100x).

Table I

Summary laboratory values at baseline and day-7 post-surgery by group

	Baseline N = 11	SBDL N=4	CBDL N=4	ΔCBDL v. SBDL p-value
Weight (g)	417 (14.5)	402.0 (9.3)	353.0 (23.5)	0.03
Total Bilirubin (mg/dl)	0.3 (0.04)	0.3 (0.0)	7.8 (3.4)	0.02
Albumin (g/dl)	4.8 (0.3)	4.9 (0.5)	2.6 (0.8)	0.03
Total Protein (g/dl)	6.3 (0.5)	6.7 (0.3)	5.4 (1.0)	0.19
Globulin (g/dl)	1.5 (0.3)	1.8 (0.4)	2.1 (1.4)	0.31
Alanine Aminotransferase (U/L)	66.4 (32.7)	52.3 (7.6)	97.0 (56.1)	1.00
Alkaline Phosphatase (U/L)	310.2 (89.4)	263.5 (69.4)	331.3 (162.5)	0.77
Creatinine (mg/dl)	0.4 (0.08)	0.3 (0.08)	0.5 (0.05)	0.21
BUN (mg/dl)	13.8 (1.7)	13.3 (1.3)	28.5 (21.8)	0.88
Sodium (mmol/L)	138.5 (2.3)	142.8 (4.1)	145.3 (11.6)	0.88
Potassium (mmol/L)	6.2 (0.8)	5.7 (0.7)	7.4 (2.8)	0.60
Calcium (mg/dl)	10.4 (0.4)	10.3 (0.3)	10.6 (2.6)	0.88
Phosphorus (mg/dl)	8.6 (0.8)	8.4 (1.5)	10.4 (5.8)	0.88

All values mean ± SD